Article

Improvement of the Torque-speed Performance and Drive Efficiency in an SRM Using an Optimal Torque Sharing Function

Wei Ye [1],*, Qishuang Ma [1] and Poming Zhang [1]

[1]   School of Automation Science and Electrical Engineering, Beihang University, Beijing, China

*   Correspondence: yewei304@buaa.edu.cn; Tel.: +86-134-3976-4637

Abstract: In this paper, by evaluating extreme value of the qth-power current, a torque sharing function (TSF) family for reducing the torque ripples in the switched reluctance motor (SRM) is proposed. The optimization criteria of the TSF has two secondary objectives, including the maximization of the torque-speed range and the minimization of copper loss. The evaluation indices in terms of the peak phase current, the rms phase current, and the torque ripple factor are compared between the proposed TSF family and four conventional TSFs including linear, sinusoidal, exponential, and cubic TSFs. An optimization objective function that combines the maximum absolute value of the rate-of-change of the flux linkage (MAV-RCFL) and the qth-power of current is proposed and a weighting factor is used to balance the influence of the two optimization objectives. An optimal TSF can be easily obtained by solving the optimization problem from the TSF family. The proposed TSF is validated by using simulations and experiments with a three-phase 6/4 SRM with 7.5 kW, 3000 rpm, and 270 V DC-link voltage. The dynamic simulation model is implemented in Matlab/Simulink. The results demonstrate the validity and superiority of the proposed control method; the optimal TSF provides better torque-speed performance, and a better reduction in copper loss and torque ripples at high speed compared to the conventional TSFs obviously.

Keywords: switched reluctance motor (SRM); torque-speed performance; drive efficiency; torque sharing function (TSF)

1. Introduction

Switched reluctance motors (SRM) are gaining interest in various applications such as electric vehicle driving system, starter-generators system, and power supply for aerospace applications, because the SRM has many advantages compared with other motors due to its low cost, durability, simple structure and robust construction [1,2]. Due to advances in high speed digital signal processing and power electronics technology, the controllable performance of the SRM has been improved greatly. However, one of the main drawbacks of the SRM used in servo-control is its large torque ripple, which leads to acoustic noise and vibration, thus cause the body vibration, transmission system parts damaged, excessive bearings wear and even axis broken accidents [3,4].

There are two main methods to reduce the torque ripple: one is to optimize the structure and magnetic design of the motor, and the other is to adopt the advanced control algorithm [5]. By optimizing the stator/rotor pole structures and the magnetic design, the torque ripple cannot be fully reduced but the cost of the motor increases [6]. The main operating parameters of an SRM include the supply voltage, the turn-on and turn-off angles, the current level, and the shaft torque. And the control algorithm is based on selecting an optimum combination of these parameters [7, 8]. Therefore,

43   an appropriate design for achieving a high SRM performance must take these factors into
44   consideration and make an optimal choice.
45   As an effective method for torque ripple reduction, direct instantaneous torque control (DITC)
46   gained interest during the last few years due to its simple control structure, which provides greater
47   flexibility for the torque ripple reduction [9-12]. However, its implementation is not easy because it
48   requires complex switching rules, uncontrolled switching frequency, and high sampling rates. In [9,
49   10], an iterative learning method for generating the optimized current waveforms was presented. In
50   [11, 12], an online DITC technique that operates without torque profile functions and auxiliary phase
51   commutating strategies was demonstrated. The optimal turn-on and turn-off angles for minimizing
52   the torque ripple or the energy consumption have been described in [13-15]. In [16], a direct torque
53   control based on the Lyapunov function was selected to minimize the torque ripples. In [17] and [18],
54   the machine design was combined with the control algorithms in an innovative method of profiling
55   the phase currents to reduce the torque ripples of an SRM.
56   The torque sharing function (TSF) is an important and effective approach for minimizing the
57   torque ripple in an SRM in the latest research [19-24]. Common TSFs curves contain linear, sinusoidal,
58   exponential, cubic curves, and so on. In order to reduce the torque ripple, the phase current product
59   the individual phase torque harmoniously using the most suitable TSFs so that the total torque can
60   be agreed with the expected torque. Subsequently, the phase torque reference can be translated into
61   the phase current reference based on the T-i-θ characteristics. With increasing speed of the SRM, the
62   phase current cannot ideally follow its reference because of the limited phase voltage and therefore
63   the torque ripples increase. In addition, because the phase current reference can be derived from the
64   phase torque reference, the choice of the TSF directly affects the copper loss and the current tracking
65   performance. The current tracking performance should be improved to enhance the torque-speed
66   capability. Thus, in order to obtain an optimum TSF, it is necessary to consider a secondary objective
67   that includes the maximization of the torque-speed range and the minimization of copper loss. These
68   two evaluation criteria affect the torque-speed performance and the drive efficiency of the motor. In
69   [19], four conventional common TSFs were studied and evaluated after optimization. In order to
70   minimize the rms (root mean square) phase current and the maximum absolute value of the rate-of-
71   change of the flux linkage (MAV-RCFL), the turn-on and the overlap angle were extracted based on
72   a genetic algorithm optimization method to select the optimal TSF. In [20], for reducing the losses of
73   the switched reluctance motors, a piecewise cubic TSF is optimized with six degrees of freedom. In
74   [21], an offline TSF with a wide torque-speed range for reducing torque ripple in an SRM was studied;
75   the objective function adopted a Tikhonov factor among two objectives to minimize the maximum
76   absolute value of RCFL and the copper loss. In [22], an extended-speed low-ripple torque control in
77   two modes using the TSF in an SRM was introduced. Because of the imperfect tracking of the phase
78   current in high motor speed, a proportional-integral controller with a torque-compensation was
79   added to the torque reference during the commutation range of two adjacent phases. In [23], a novel
80   and simple nonlinear logical TSF was proposed to reduce the torque ripple and improve the
81   efficiency. The logical TSF was used online and was not fixed compared with the other TSFs. The
82   incoming phase current was controlled in a ladder-like increase, and the current of the outgoing
83   phase was tracked in the opposite direction. Therefore, torque sharing between the incoming and
84   outgoing phases was achieved with a minimum current crossover. However, a theoretical analysis of
85   the RCFL was not provided for this study.
86   In this paper, taking into account the requirements for the maximization of the torque-speed
87   range and the minimization of copper loss and balancing these secondary objectives by including a
88   weighing factor, a family of TSFs deduced by an invertible torque function is proposed. Because the
89   proposed TSF provides phase currents throughout the whole region, the torque-speed capability is
90   improved as well. The solution of the TSFs selection becomes a muti-objective optimization problem.
91   And then, the evaluation indices such as the peak phase current, the rms phase current, and the
92   torque ripple factor are compared between the proposed and the classical TSFs by using a simulation.
93   Finally, the simulation and experimental results show that the proposed control algorithm has
94   advanced performance in reducing the copper loss and improving torque-speed performance.

2. The Finite Element Method Analysis for the SRM

The SRM only has stator windings. no rotor windings or magnets. The whole or part of each phase is comprised of two stator windings on diametrically opposite sides of the SRM. A three-phase 6/4 SRM with 7.5kW, 3000rpm, and 270V DC-link voltage is designed (seen Table A1 in Appendix A). Figure 1 (a-d) shows the analysis model of the studied motor using the finite element method (FEM) with the magnetic flux at rotor positions of 0°, 15°, 30°, and 45° respectively. The anti-clockwise is the positive direction of the rotor angular position θ and the alignment position of the stator and rotor poles is defined as 0°.
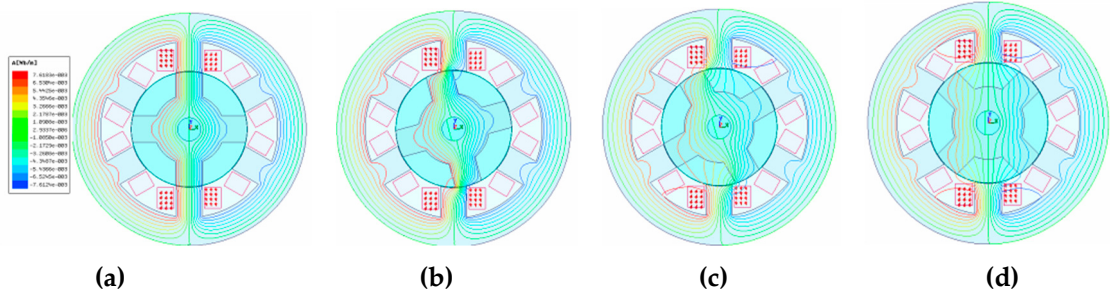

(a)　　　　　　**(b)**　　　　　　**(c)**　　　　　　**(d)**

Figure 1. The FEM analysis model of the SRM with the magnetic flux (I=8A): **(a)**θ=0°; **(b)**θ=15°; **(c)**θ=30°; **(d)**θ=45°.
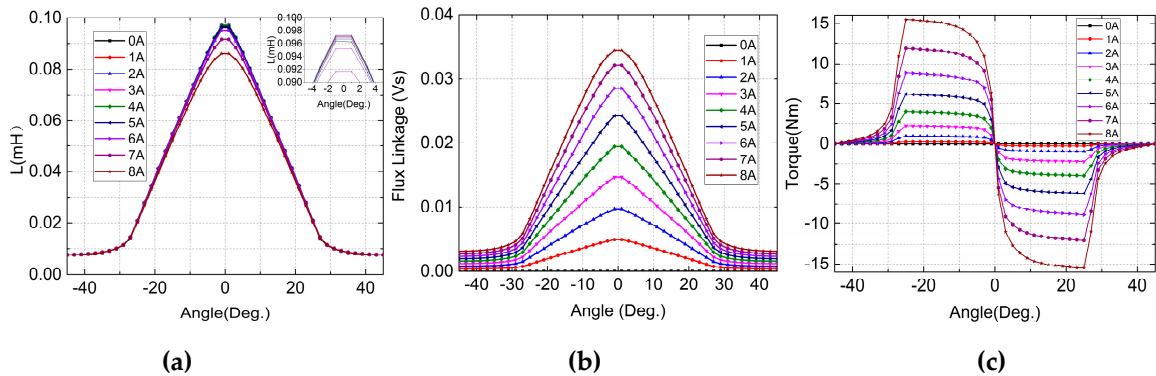

(a)　　　　　　　　**(b)**　　　　　　　　**(c)**

Figure 2. The phase inductance, the flux linkage profiles and the torque characteristics of the studied SRM: **(a)** inductance profiles; **(b)** flux linkage profiles; **(c)** torque profiles.

In practical SRM analysis, the non-linear characteristics and the electromagnetic analysis of the SRM are important. By using ANSOFT/Maxwell software, the flux linkage, the phase inductance profiles and the torque characteristics of the studied SRM were analyzed. And the results are shown in Figure 2 (a)-(c). Due to the saturation effect, the maximum value of the phase inductance decreases with the increase of the current. In Figure 2 (b), the flux linkage characteristics demonstrate the saturation effects. The lowest curve corresponds to a 0 A phase current and the top of the curve to a 8A phase current. The torque generated by a constant current and a ±45° in the phase-A winding is shown in Figure 2 (c) and is the same as the other phases. The phase torque has nonlinear properties which strongly depends on the phase current values and the rotor position. It is significant that the phase torque decreases when the rotor position is near the alignment position of the stator and rotor poles. This is caused by the saturation effect, which leads to a decrease in the derivative of the co-energy to the rotor position. This, in turn, cause the large torque ripple of the SRM, which requires a complex control strategy to reduce. As shown in Figure 3 (a) and (b), the linear interpolation resulted in a surface fitting and this linear interpolation approach can be used for other non-test states to obtain the necessary data for the flux linkage and the torque for any given value (i, θ).
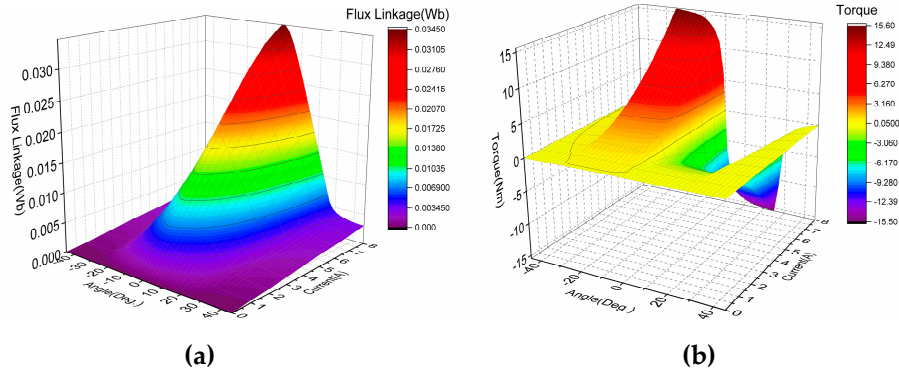
126
127 **(a)** **(b)**
128 **Figure 3.** linear interpolation results: **(a)** 3-D relationships of Ψ-i-θ; **(b)** 3-D relationships of T-i-θ.

129 **3. Theoretical Background of the SRM**

130 *3.1 Torque Generation*

131   The principle of the torque generation in an SRM is based on the reluctance minimization of the
132 magnetic flux linkage paths. each phase torque strongly varies with the phase current and rotor
133 position variation. Generally, the phase torque T_k can be calculated from the co-energy as follows:

$$T_k(i_k,\theta) = \frac{\partial \int_0^{i_k} \psi_k(i_k,\theta)di_k}{\partial \theta} \qquad k = 1,2,\cdots,m$$

134 (1)
135 where k is the identifier of the phases, θ is the rotor position, i_k is the phase current, and Ψ_k is the
136 phase flux linkage. All of the position angles refer to mechanical angles (except where noted). The
137 two basic equations that describe each phase flux linkage and the machine model of the SRM are as
138 follows

$$\psi_k(i_k,\theta) = L_k(i_k,\theta) \cdot i_k$$

139 (2)

$$u_k = R \cdot i_k + \frac{d\psi_k}{dt}$$

140 (3)
141 where L_k is the kth phase inductance, u_k is the kth phase instantaneous voltage, and R is the phase
142 winding resistance. Because of the highly nonlinear and saturation effects of the electromagnetic
143 characterization in the SRM, the inductance L_k in Eq. (2) varies not only with phase current value but
144 also with rotor position variation.
145   By neglecting the saturated nature, we simplify the formula and assume that the inductance L_k
146 varies only with the rotor position θ. According to Eqs. (1) and (2), the torque T_k can be expressed as

$$T_k(i_k,\theta) = 0.5i_k^2 \cdot \frac{dL_k(\theta)}{d\theta} = 0.5L_{kp}(\theta) \cdot i_k^2$$

147 (4)
148 where L_{kp} is denoted as the derivative of L_k. In this case, assuming that L_{kp} is known, Eq. (4) enables a
149 fast and simple torque calculation.

150 *3.2 TSFs*

151   To minimize the torque ripple, the commonly used TSFs can be classified as linear, sinusoidal,
152 exponential, and cubic and their details have been reported in [19] and [24]. Through the torque
153 control with a TSF in the region where it shares the torque with one or more phases (called the
154 commutation or overlap region), the total torque reference T_{ref} is divided into separate torque
155 reference $T_{ref(k)}$ for each phase. According to the characteristics of the torque-current-position, the $T_{ref(k)}$
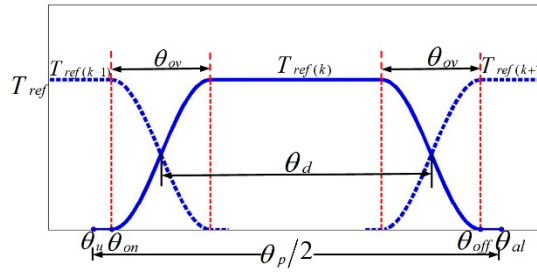156 is converted into the phase current reference i_k with respect to the rotor position information.

157
158   **Figure 4.** Illustration of a TSF.

159   Figure 4 shows an illustration of a TSF. The kth phase torque reference denoted as $T_{ref(k)}$ is
160   calculated as

$$
T_{ref(k)}(\theta) =
\begin{cases}
0 & \theta_u \leq \theta \leq \theta_{on} \\
T_{ref} \cdot f_{rise}(\theta) & \theta_{on} < \theta < \theta_{on} + \theta_{ov} \\
T_{ref} & \theta_{on} + \theta_{ov} \leq \theta \leq \theta_{off} - \theta_{ov} \\
T_{ref} \cdot f_{fall}(\theta) & \theta_{off} - \theta_{ov} < \theta < \theta_{off} \\
0 & \theta_{off} \leq \theta \leq \theta_{al}
\end{cases}
\tag{5}
$$

161
162   where θ_u, θ_{on}, θ_{ov}, θ_{off} and θ_{al} are the unaligned, turn-on, overlap, turn-off and aligned angles,
163   respectively; $f_{rise}(\theta)$ and represents the ascending area and $f_{fall}(\theta)$ represents the descending area in the
164   TSF. In the commutation region, $f_{rise}(\theta)$ must increase from 0 to 1 and $f_{fall}(\theta)$ must decrease from 1 to
165   0. For any TSF, the function $f_{fall}(\theta)$ that is relevant to $f_{rise}(\theta)$ can be computed as follow

$$
f_{fall}(\theta) = 1 - f_{rise}(\theta + \theta_{on} + \theta_{ov} - \theta_{off})
\tag{6}
$$

166
167   The angle $\theta_p = 2\pi/N_r$ denotes the rotor pole pitch, where N_r is the number of rotor poles. And
168      $\theta_d = 2\pi/(mN_r)$ denotes the angular displacement between the neighboring phases. In the case of a
169   normal SRM commutation, these angles have the following relationships:

$$
\theta_{al} - \theta_u = \theta_p/2
\tag{7}
$$

170

$$
\theta_{ov} = \theta_{off} - \theta_{on} - \theta_d \leq \theta_p/2 - \theta_d
\tag{8}
$$

171
172   Thus, we can get $\theta_p=90°$, $\theta_d=30°$, and $\theta_{ov} \leq 15°$ from Eq. (7) and (8) in the three-phase 6/4 SRM. For
173   the four-phase 8/6 SRM, we have $\theta_p=60°$, $\theta_d=15°$, and $\theta_{ov} \leq 15°$.

174   **4. Evaluation Criteria**

175   *4.1 The MAV-RCFL*

176   Materials and Methods should be described with sufficient details to allow others to replicate
177   and build on published results. Please note that publication of your manuscript implicates that you
178   must make all materials, data, computer code, and protocols associated with the publication available
179   to readers. Please disclose at the submission stage any restrictions on the availability of materials or
180   information. New methods and protocols should be described in detail while well-established
181   methods can be briefly described and appropriately cited.
182   The MAV-RCFL is easily obtained from Eq. (3). At a steady state of non-zero angular speed and
183   neglecting the phase resistance, Eq. (3) can be represented as follows, where V_{dc} is the phase DC-link
184   voltage:

$$
\frac{d\psi_k}{d\theta} = \frac{V_{dc}}{\omega}
\tag{9}
$$

185
186   It is evident that the MAV-RCFL depends on the phase DC-link voltage V_{dc} and the rotor angular
187   speed ω with respect to the position θ. That means that, for a given V_{dc}, the flux linkage derivatives
188      $d\Psi_k/d\theta$ can estimate the rotor speed range at which the torque-speed performance theoretically allows
189   a torque-ripple-free operation. It can be seen from Eq. (9) that the maximum absolute value of $d\Psi_k/d\theta$
190   limits the maximum speed range ω_{max}. The MAV-RCFL denoted as M_R is defined as

$$M_R = \max_{\theta_{on} \leq \theta \leq \theta_{off}} \left\{ \left| d\Psi_k / d\theta \right| \right\}$$

(10)

According to Eqs. (9) and (10), the maximum speed range ω_{max} for operating torque ripple performance freely must satisfy

$$\omega_{max} \leq \frac{V_{dc}}{M_R}$$

(11)

To be specific, the smaller the maximum M_R, the larger the maximum rotor speed ω_{max} is. In other words, the MAV-RCFL is expected to be as small as possible.

4.2 Copper Loss

Total losses in an SRM include iron loss and copper loss and the latter represent the major component of the losses. Thus, the copper loss directly influences the torque-speed performance and the drive efficiency. And the copper loss is in direct proportion to the square value of the rms phase current I_{rms}, which is calculated from:

$$I_{rms}^2 = \frac{1}{\theta_p} \int_{\theta_{on}+\theta_{ov}}^{\theta_{off}-\theta_{ov}} i_k^2(\theta) d\theta + \frac{1}{\theta_p} \int_{\theta_{on}}^{\theta_{on}+\theta_{ov}} \left[i_k^2(\theta) + i_{k-1}^2(\theta) \right] d\theta$$

(12)

Since in the region $\theta_{on}+\theta_{ov} \leq \theta \leq \theta_{off} - \theta_{ov}$, the kth phase produces the total torque independently as shown in Figure 4 and minimizing the rms phase current I_{rms} can be realized by decreasing the second part of Eq. (12).

Hence, by modifying Eq. (12), an optimization objective function can be expressed as follow:

$$\min: J_1 = i_k^q(\theta) + i_{k-1}^q(\theta)$$

(13)

where q is a bound variable satisfied $q \geq 2$. In Eq. (13), the qth-power of the current is a substitute for the integration of the averaged square value of the current during the commutation.

A torque reference profile can now be generated for a specific TSF. The current profile and the flux linkage profile are obtained using the given torque and flux-linkage characteristics. Hence, the MAV-RCFL and the square value of the rms current can be computed. As discussed above, by optimizing the TSFs, a wide rotor speed range and less copper loss can be obtained by minimizing the MAV-RCFL and the square value of the rms current. This is the basic principle and direction for selecting an optimal TSF.

5. Proposed TSFs

5.1 Optimization Objective for Proposed TSF

An optimization objective function that combines MAV-RCFL M_R and the qth-power of current J_1 with a weighting factor is proposed as

$$\min: J = w_f \overline{J}_1 + (1 - w_f) \overline{M}_R$$

(14)

where w_f is the weighting factor satisfied $0 \leq w_f \leq 1$. $\overline{J}_1$ and $\overline{M}_R$ are the normalized values of J_1 and M_R respectively and they can be computed from $\overline{J}_1 = J_1 / J_{1,max}$ and $\overline{M}_R = M_R / M_{R,max}$, where $J_{1,max}$ and $M_{R,max}$ are the maxima of J_1 and M_R respectively.

When $w_f = 1$, the proposed optimization objective function only consists of the square value of the rms current. In this case, the minimum copper loss is the only optimization objective. When $w_f = 0$, the maximum speed range is the only optimization objective. When $0 < w_f < 1$, both maximum speed range and minimum copper loss at different proportion are considered as the optimization objectives in order to obtain the correct balance.

5.2 A Family of TSFs

According to the definition of a TSF from Eqs. (5) and (6), the phase torques produced by the currents $i_k(\theta)$ and $i_{k-1}(\theta)$ in Eq. (13) share the total torque reference in the commutation region, which are denoted as $T_{ref(k)}(\theta)$ and $T_{ref(k-1)}(\theta) = T_{ref} - T_{ref(k)}(\theta)$. Thus, by neglecting the saturated effects, Eq. (13) can be rewritten from Eq. (4) as

$$J_1 = \left[\frac{T_{ref(k)}}{0.5 L_{kp}(\theta)} \right]^{q/2} + \left[\frac{T_{ref} - T_{ref(k)}}{0.5 L_{k-1p}(\theta)} \right]^{q/2}$$

(15)

234

235   When dJ_1/d$T_{ref(k)}$=0 to obtain the extreme value of J_1, the desirable TSF calculated from Eq. (15) is
236   depicted as

$$T_{ref(k)} = T_{ref} \cdot \frac{1}{1 + \left[L_{k-1p}(\theta) / L_{kp}(\theta) \right]^r}$$

(16)

237

238   where $r=q/(q-2)$ is an undetermined constant satisfied $r \geq 1$. $T_{ref} \cdot f_{rise}(\theta)$ in Eq. (5) is defined by the right
239   part of Eq. (16) and the other section of TSF can be easily obtained from Eq. (6).

240   *5.3 Comparison of the Conventional and Proposed TSFs*

241   Figure 5 shows the typical profiles of four common conventional TSFs. The turn-on angle, turn-
242   off angle, and overlap angle, θ_{on}, θ_{off}, and θ_{ov} are set to 5°, 40° and 5°, respectively. And the torque
243   reference T_{ref} is set to 1 Nm. In Figure 5(a)-(d), the profiles (top to bottom) are the torque reference,
244   the current reference, the flux linkage reference, and the absolute value of RCFL respectively. From
245   Figure 5 (d), the values of M_R for the linear, sinusoidal, exponential, and cubic TSFs are 11.78, 6.75,
246   5.05, and 19.10 Wb/rad, respectively. According to Eq. (11), the values of maximum rotor speed ω_{max}
247   for a torque-ripple-free operation of four common conventional TSFs are 22.9, 40, 53.5, and 14.1 rad/s,
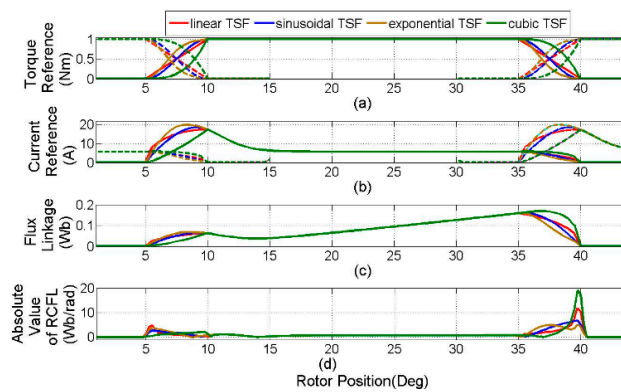248   which are equal to only 219, 382, 511, and 135 rpm, respectively
249   .

250
251   **Figure 5.** Typical profiles of four conventional TSFs.

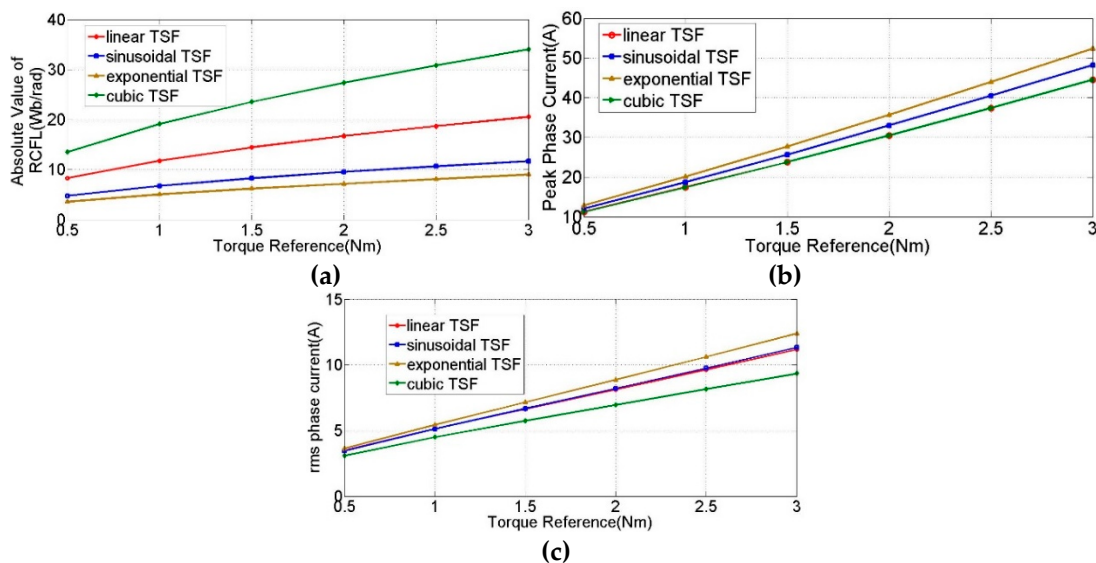252
253   **(a)**   **(b)**

254
255   **(c)**
256   **Figure 6.** Comparison of four conventional TSFs: **(a)** absolute value of the RCFL; **(b)** peak phase current; **(c)** rms
257   phase current.

258   Figure 6(a) shows the change in the MAV-RCFL with the changing torque reference, indicating
259 that the exponential TSF resulted in the lowest RCFL value. The peak values of the reference currents
260 at each torque reference are compared in Figure 6(b) showing an increase in the currents as the torque
261 reference increases. The peak current is the same for the linear TSF and the cubic TSF and it is lower
262 than for the other two TSFs. This indicates that the power converter has much smaller pressure and
263 better insulation for the linear and cubic TSFs. The rms currents at each torque reference are
264 compared in Figure 6(c), which indicates that the linear and the sinusoidal TSFs have almost the same
265 value of rms current at the torque reference between 0.5Nm and 3Nm. The rms current is lower for
266 cubic TSF than for the other TSFs.
267   In summary, if the minimum M_R (when w_f =0 in Eq. (14)) is the only optimization target, the best
268 choice of TSF is the exponential TSF, the second best choice is the sinusoidal TSF, and the worst choice
269 is the cubic TSF. On the other hand, if the minimum copper loss J_1 (when w_f =1 in Eq. (14)) is the only
270 optimization objective, the cubic TSF represents a good choice, and it also has the lowest value for
271 the peak current.
272   Figure 7 (a-d) show the typical profiles of several proposed TSFs for different r values. From
273 Figure 7, when r tends to ∞, the minimization of the copper loss is achieved theoretically because the
274 torque reference tends to be zero during the commutation region. By decreasing r, the torque
275 reference increases during the commutation region, which results in an increase in the rms phase
276 current. When r tends to 1, Figure 7(b) shows that the phase current reference of two adjacent excited
277 phases in the commutation region is equal. And it is clear that the peak value of phase current is also
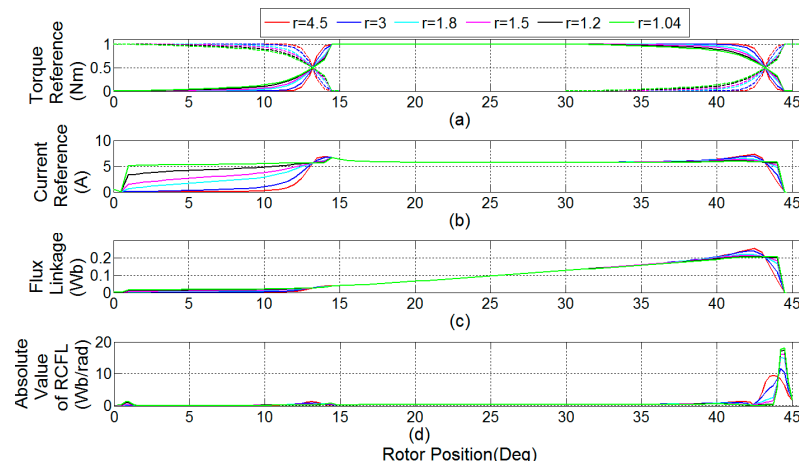278 the smallest when the TSF is defined by $r→1$.

279
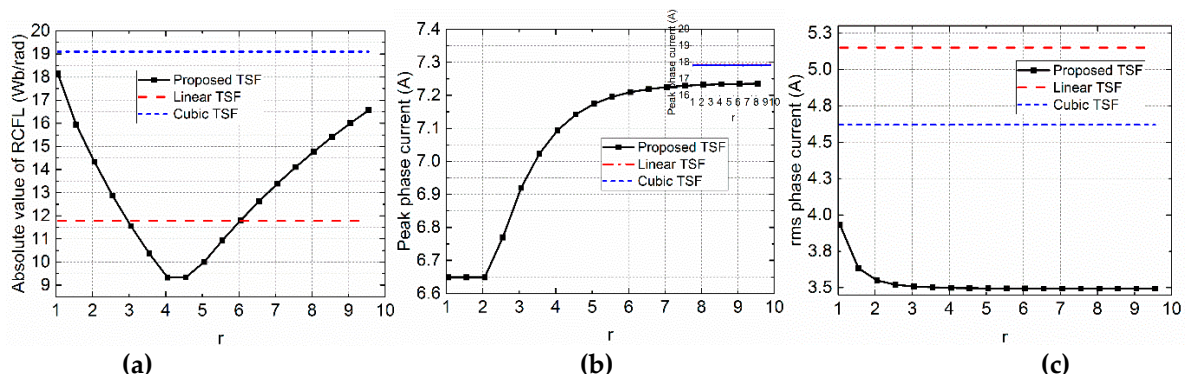280 **Figure 7.** Typical profiles of the proposed TSF family.

281
282   **(a)**   **(b)**   **(c)**
283 **Figure 8.** Comparison of the proposed TSFs: **(a)** absolute value of the RCFL; **(b)** peak phase currents; **(c)** rms
284 phase currents.

285   Figure 8(a) shows the relationship between the MAV-RCFL and the exponent r. As M_R reaches
286 its minimum at $r≈4$, it is reasonable to choose $r=4$ as the exponent of the optimal TSF in Eq. 16.   When
287 T_{ref} is set to 1 Nm and V_{dc} is set to 270V in the case of $r=4$, the maximum speed range ω_{max} for operating
288 torque ripple performance freely can be achieved at 30 rad/s, which is equal to 286.6 rpm. The

289   equivalent level of the linear and the cubic TSFs are also marked with the dash-dotted line in the
290   Figure 8 (a-c) for comparison. Figure 8(b) shows the peak phase current reference as a function of the
291   exponent *r*. If *r* is larger than 3.5, the peak phase current exceeds the theoretical minimum value of
292   6.65 A by more than 5%. In Figure 6(b), the minimum peak current values of the four common
293   conventional TSFs are about three times higher than the values of the proposed TSFs. The rms phase
294   current reaches a theoretical minimum value of 3.5 A when $r\geq3$ from Figure 8(c). Assuming a torque
295   reference of 1 Nm, the rms current values are larger for the four common conventional TSFs than for
296   the proposed TSFs at any value of *r* (Figure 6(c)).
297   Therefore, the TSF with the minimum M_R value at *r*=4, denoted as TSF1 (*r*=4), should be used as
298   the optimal value at higher speed because it provides smaller peak phase current and lower copper
299   loss relatively.

6. Nonlinear Mathematical Model of Torque Profile

301   The optimal TSF is obtained by solving the optimization problem in Eq. (14). However, Eq. (4)
302   is utilized to approximate the phase torque based on a linear relationship between the phase flux
303   linkage and the current as shown in Eq. (3). An analytic invertible torque function that represents the
304   nonlinear and saturation effects appropriately was used as follows [26]:

$$T_k(\theta,i) = \frac{1}{2}\frac{L_{kp}(\theta)i^2}{(1+f(\theta)i^n)^{1/n}}$$

(17)

306   where $L_{kp}(\theta)$, $f(\theta)$ and n are the undetermined parameters that are dependent on the rotor position
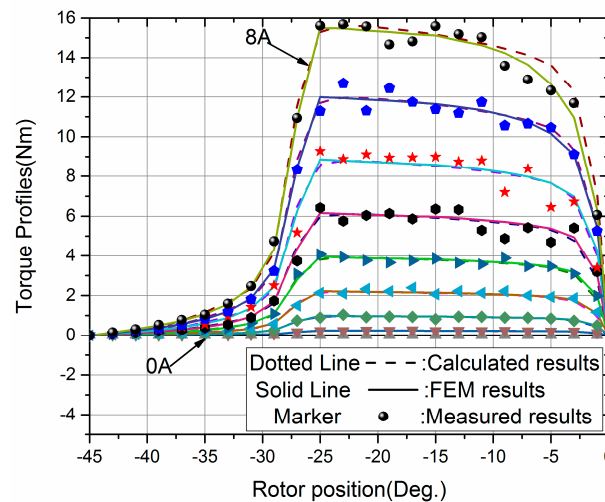307   and the motor parameters.

Figure 9. Comparison of the calculated, FEA, and measured static torque characteristics for 0 to 8 A with an increment of 1 A.

311   As shown in Figure 9, by choosing reasonable parameters for $L_{kp}(\theta)$ and $f(\theta)$, the characteristics
312   of the torque-current-position obtained from Eq. (17) agree well with those using FEA or those from
313   experimental measurements. After rejecting the improbable solution, the current reference can be
314   rewritten as Eq. (18) by inverting the torque equation in Eq. (17) as follows:

$$i_k(\theta,T_k) = \frac{2T_k}{L_{kp}(\theta)}\left[\frac{f(\theta)}{2}+\sqrt{\frac{f^2(\theta)}{4}+\left(\frac{L_{0p}(\theta)}{2T_k}\right)^n}\right]^{1/n}$$

(18)

316   The data of the two angular functions $L_{kp}(\theta)$ and $f(\theta)$ stored in the digital controller can be used
317   to calculate the current reference according to Eq. (18), instead of using the 3-D lookup table of T-i-θ.

7. Simulation Results and Comparison

319   Figure 10 shows the block diagram of the torque control using the TSF method for the studied
320   SRM. The individual phase torque reference is defined from the total torque reference by the TSF

321   block. In the "Torque-to-Current" block, the phase torque references are converted into phase current
322   references the rewritten torque-current profile model of the SRM (Eq. (18)). A hysteresis current
323   controller is used for the phase current tracking its reference waveforms.
324   Matlab /Simulink was used to for the simulation model of the three-phase 6/4 SRM with 7.5 kW,
325   3000 rpm, and 270 V DC-link voltage by using the static torque characteristic profiles shown in Figure
326   9 and obtained using Eq. (17). For the phase current tracking its reference waveforms accurately, it is
327   appropriate to set the hysteresis band of the current controller to ±0.1 A through simulation test. The
328   phase current reference is calculated using Eq. (18). The same sampling time t_{sample}=1μs is set in all
329   simulation. Finally, the evaluation indices in terms of peak phase current, rms phase current, and
330   torque ripple factor are compared between the proposed and the classical TSFs.
331   The torque ripple factor is defined as follows:

$$T.R\% = \frac{T_{max} - T_{min}}{T_{ave}} \times 100\%$$

332
333   where T_{max}, T_{min}, and T_{ave} are the maximum, minimum, and average torque, respectively.   (19)
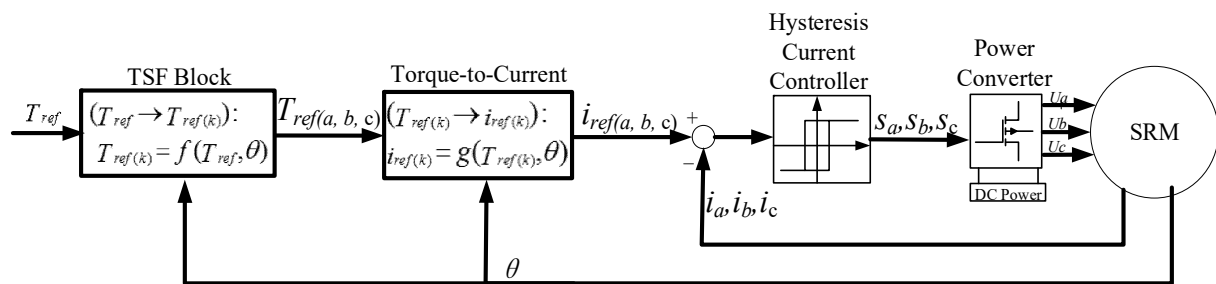

334
335   **Figure 10.** Block diagram of the torque control using the TSF method.

7.1 Simulation Results

337   The CCC (current chopping control) method is common in the SRM control and was investigated
338   in [27]. The simulation results for the proposed TSF1 (r=4) are compared with the CCC and the
339   conventional TSFs at a torque reference T_{ref}=1.5 Nm and a rotor speed of 1000 rpm (Figure11 (a)-(d)).
340   Since the rotor speed 1000 rpm of all TSFs is higher than the maximum rotor speed ω_{max}, the phase
341   current cannot track its reference. The torque ripple factors T.R% for the CCC, the linear, sinusoidal,
342   and the proposed TSFs are 116.7%, 28.7%, 22.0%, 23.5%, respectively. The rms currents are 3.5 A for
343   the linear and sinusoidal TSFs, and 3 A for the TSF1 (r=4).
344   The simulation results for the CCC, the linear, the sinusoidal, and the proposed TSFs at a torque
345   reference of T_{ref}=1.5 Nm and a speed of 3000 rpm are shown in Figure 12 (a)-(d). As the rotor speeds
346   up, the phase current deviates from its reference significantly during the current rising region. And
347   the phase current exhibits a tail phenomenon at the same time during the current declining region.
348   Therefore, the output torque cannot track its reference accurately and the torque ripple increases
349   obviously. The torque ripple factors *T.R*% are 182.3%, 61.3%, 60.8%, and 36.6%, respectively. For the
350   CCC, the linear, the sinusoidal, and the proposed TSF1 (r=4), the peak phase currents are 8.8 A, 9.4
351   A, 9.5 A, and 5.5 A, and the rms phase currents are about 5.4A, 5.4A, 5.3A and 3.8A, respectively. It
352   is evident that the CCC method results in a comparatively smaller peak phase current compared with
353   the conventional TSFs. However, the torque ripple is not acceptable because it is three times higher
354   than that of the proposed TSF1 (r=4). The linear and sinusoidal TSFs almost have the same
355   performance with regard to the torque ripple and the peak phase current, which is approximately
356   twice as high as those for the proposed TSF1 (r=4). The proposed TSF1 (r=4) results in the lowest
357   torque ripple, which is 1/2 of the torque ripple of the linear TSF. In addition, the required phase
358   current is lower than for the CCC. The control performance is clearly improved by using the proposed
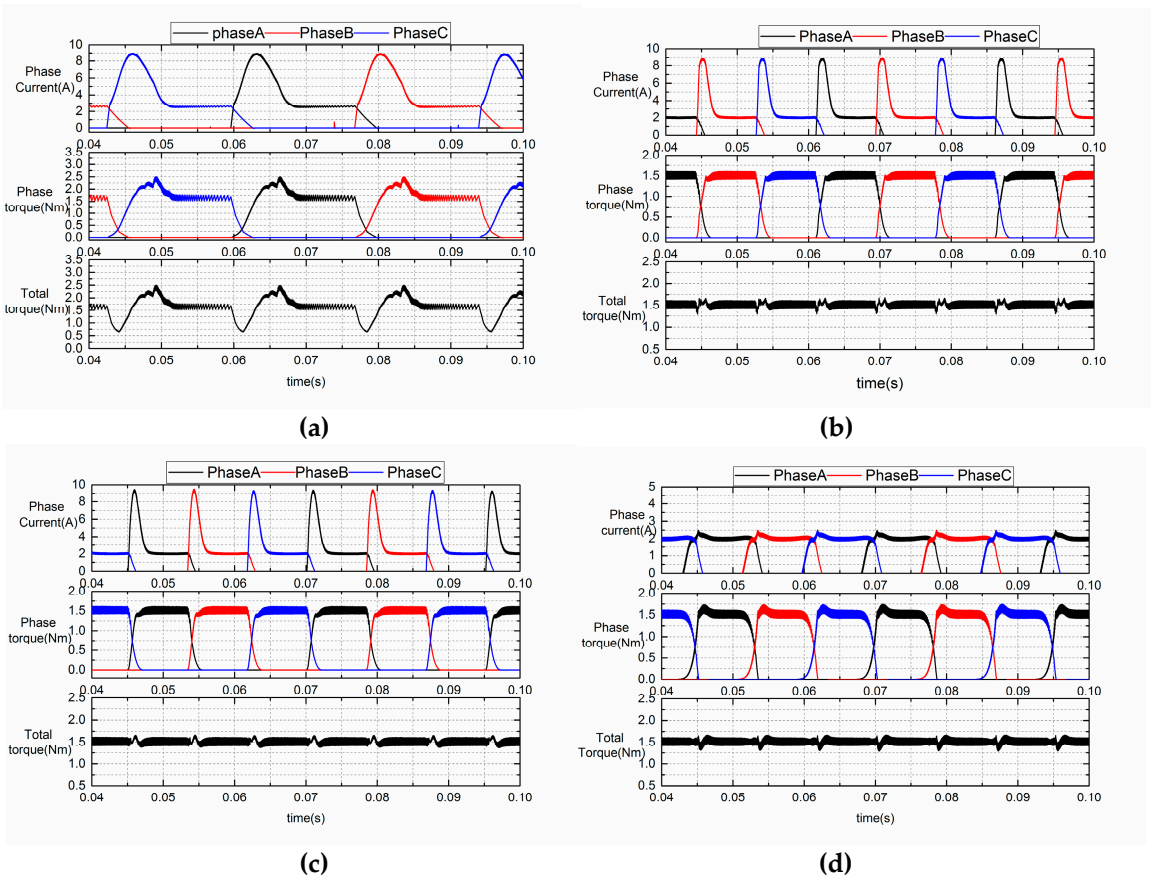359   TSF1 (r=4).

Figure 11. Simulation results (T_{ref}=1.5 Nm, 1000 rpm): **(a)** CCC; **(b)** Linear TSF; **(c)** Sinusoidal TSF; **(d)** TSF1 (*r*=4).
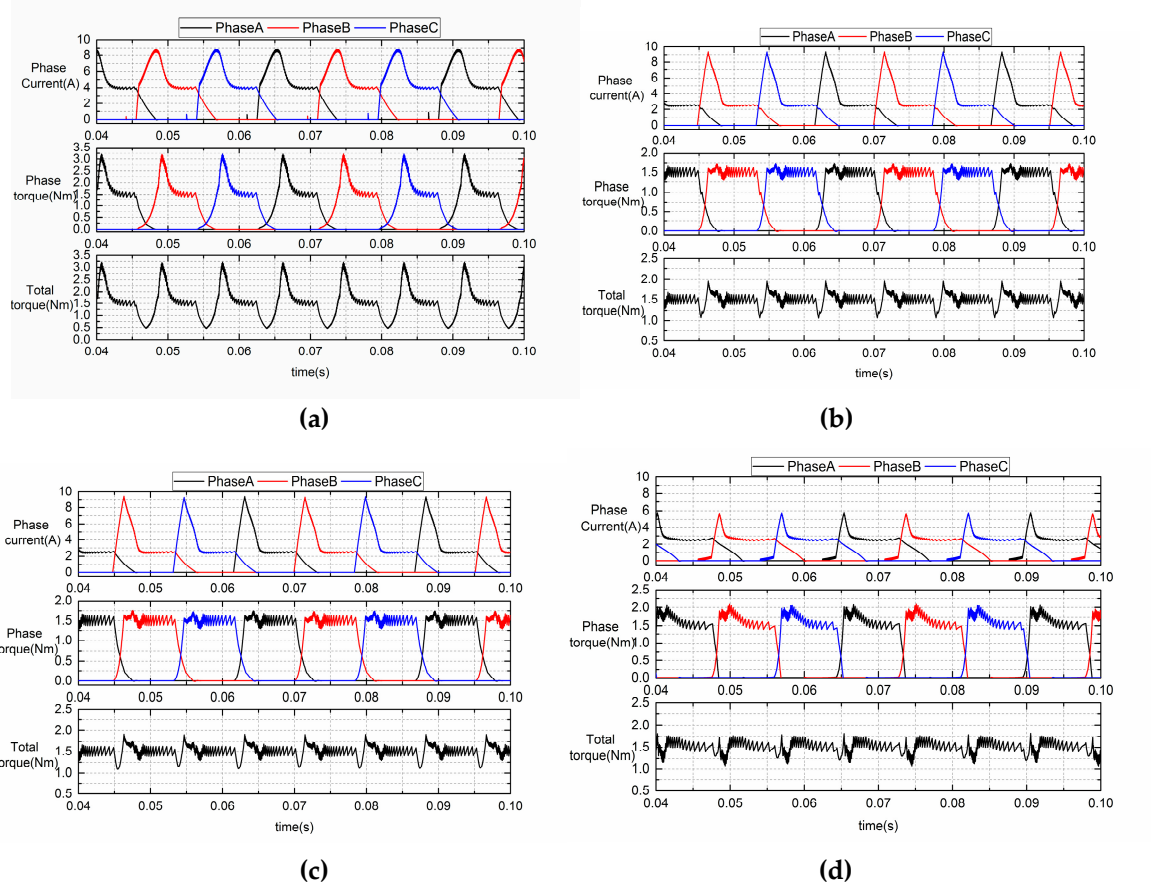

Figure 12. Simulation results (T_{ref}=1.5 Nm, 3000 rpm): **(a)** CCC; **(b)** Linear TSF; **(c)** Sinusoidal TSF; **(d)** TSF1 (*r*=4).

370   *7.2 Comparison of the Simulation Results*

371   Figure 13(a) shows the comparison results of the torque ripple between the CCC, the linear, the
372   sinusoidal, and the proposed TSF1 (*r*=4) when the torque reference is set to 1.5 Nm. The CCC is the
373   worst choice in all methods. For the conventional TSFs, the torque ripples are almost two to three
374   times higher at 3000 rpm than at 1000 rpm. And at 3000rpm, the torque ripple of the proposed TSF1
375   (*r*=4) is nearly one half of the other TSF methods. That means the proposed TSF1 (*r*=4) have a better
376   performance than the other control method. Actually at a lower rotor speed, the torque ripple of the
377   proposed TSF is obviously affected by the hysteresis band of the current controller. Therefore, the
378   torque ripple can be decreased further more by reducing the inherent current ripple of the hysteresis
379   controller.

380   Figure 13 (b) shows the comparison results of the rms current for all control methods and the
381   CCC is also the worst choice. At the rotor speed less than 500rpm, the proposed and the conventional
382   TSFs exhibits almost a similar rms current. As the rotor speeds up, due to the poorer current tracking
383   performance, the rms currents of the linear and sinusoidal TSFs increase significantly. However, the
384   rms current for the proposed TSF remains relatively as the speed increases.

385   The peak current is much smaller for the TSF1 (*r*=4) than those for the other methods, which
386   have smaller hardware pressure (Figure 13(c)). At a higher speed, the peak currents of the
387   conventional TSFs decrease significantly due to the poorer current tracking performance by the
388   inductance effect. Therefore, the TSF1 (*r*=4) is a better choice for reducing torque ripple and lower
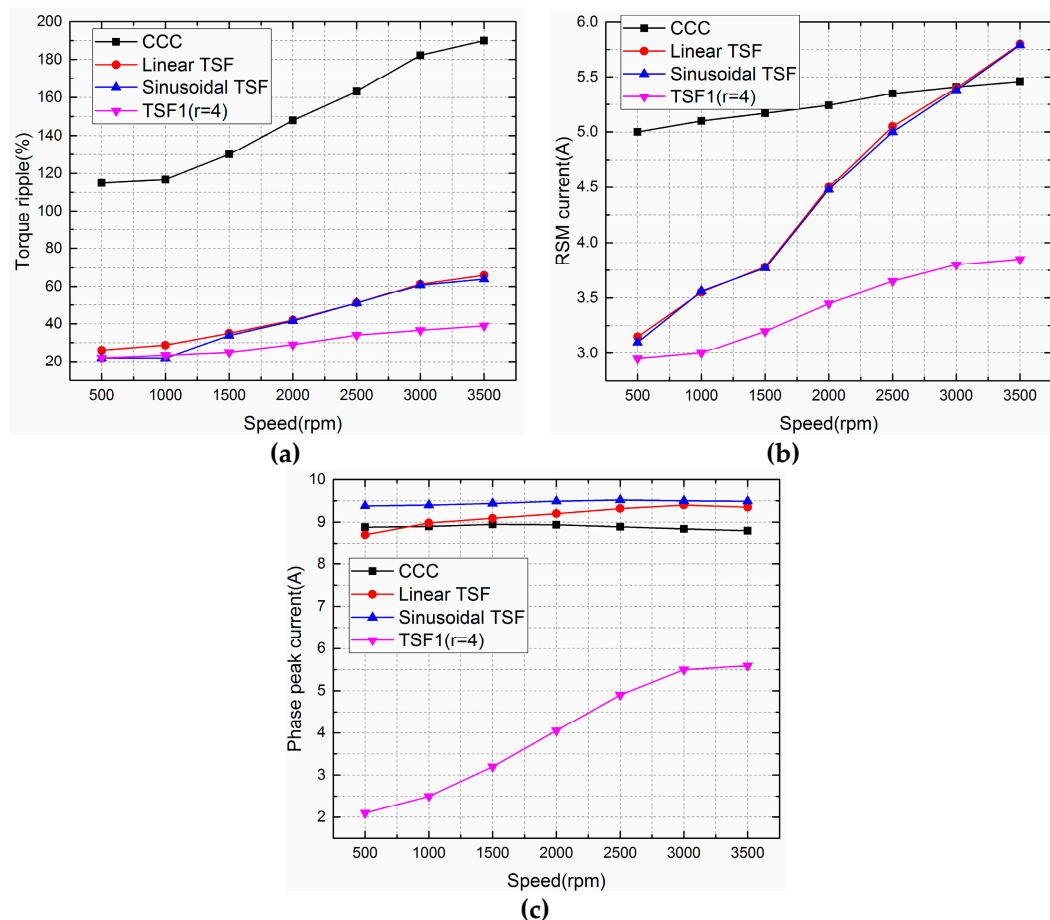389   copper loss relatively.

390
391   **(a)**   **(b)**

392
393   **(c)**
394   **Figure 13.** Comparison of CCC and different TSFs: **(a)** torque ripple; **(b)** rms phase current; **(c)** peak current.

395   Figure 14(a) and (b) show the values of the objective function *J* for different weight factors w_f at
396   speeds of 1000 rpm and 3000 rpm. It is evident that the linear TSF is the worst choice because its *J*
397   values are always much larger than those of the other TSFs at any weighting factor. The sinusoidal
398   and cubic TSFs have almost the same *J* values at a speed of 1000 rpm. However, as the speed increases,

399 the cubic TSF exhibits a better performance. At any weight factor w_f or any speed, the proposed TSF1
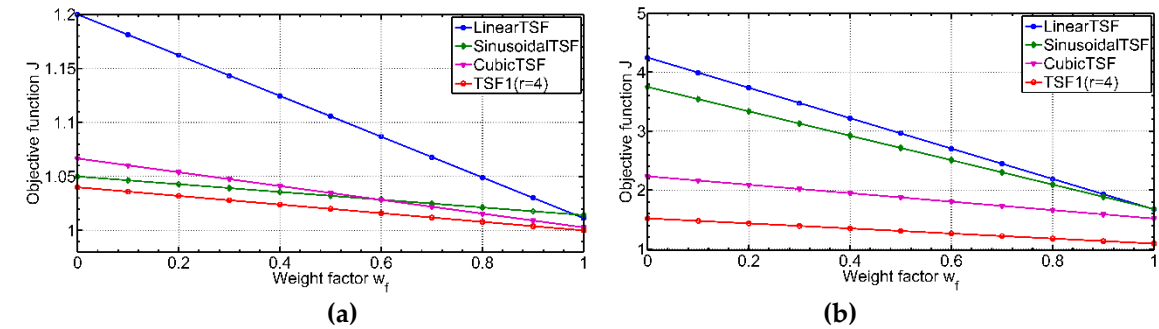400 (r=4) has the best minimum J values when compared to the sinusoidal or cubic TSFs.

401
402   **(a)**   **(b)**
403 Figure 14. The values of the objective function J at different weight factors w_f: **(a)** 1000 rpm, **(b)** 3000 rpm.

404 **8. Experimental Results**

405   The proposed TSF is validated with an experiment using a three-phase 6/4 SRM with 7.5 kW,
406 3000 rpm, and 270 V DC-link voltage (shown in Figure 15). A Texas Instruments (TI) TMS320F2812
407 digital signal processor (DSP) is used as a digital controller. The T-i-θ characteristics are stored as
408 look-up tables in the DSP. The SRM is driven by a three-phase asymmetric inverter and the motor
409 shaft is coupled with a torque-speed sensor and position sensor. There is one current sensor on each
410 phase line. A synchronous generator with a resistance box is used as the load.
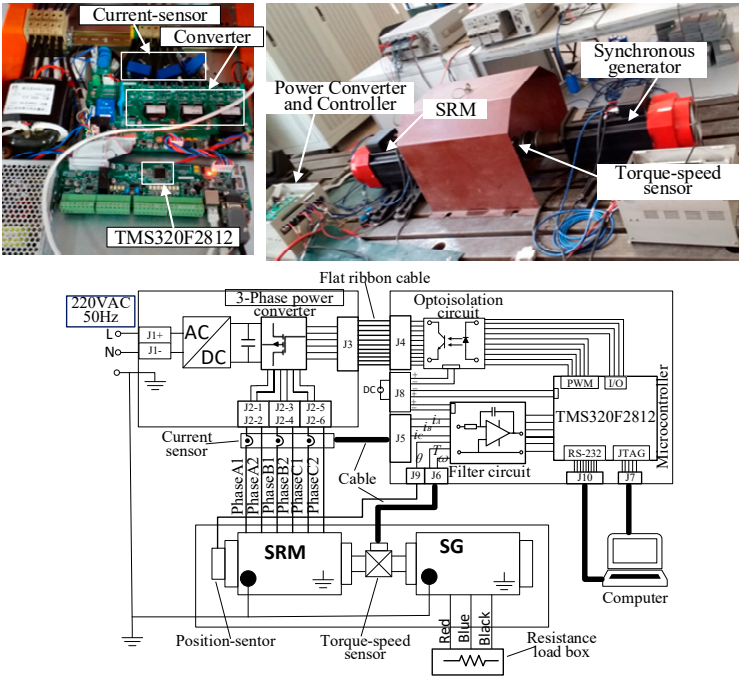

411

412
413 **Figure 15.** Experimental setup of the SRM drive system

414   Figure 16 shows the measured phase current and instantaneous torque at 3000 rpm at a torque
415 reference of T_{ref}=1.5 Nm. For the CCC, the linear TSF, the sinusoidal TSF and the proposed TSF1 (r=4),
416 the torque ripples are around 184%, 67.8%, 66.7%, and 40.4%, respectively compared to the values of
417 182.3%, 61.3%, 60.8%, and 36.6% in simulation results shown in Figure 12. And the peak phase
418 currents are 8.9 A, 9.5 A, 9.5 A, and 5.9 A, and the rms phase currents are about 5.6A, 5.4A, 5.4A and
419 3.9A, respectively. This indicates that the experimental results agree well with the results of the
420 simulation in terms of current waveforms, torque ripple and torque response under the same
421 operating conditions. Due to a current tracking error, the CCC and the conventional TSFs show much
422 higher torque ripples compared to the TSF1 (r=4), which achieves better tracking and has a nearly flat
423 output torque, ignoring the torque ripple caused by the inherent current ripple of the hysteresis
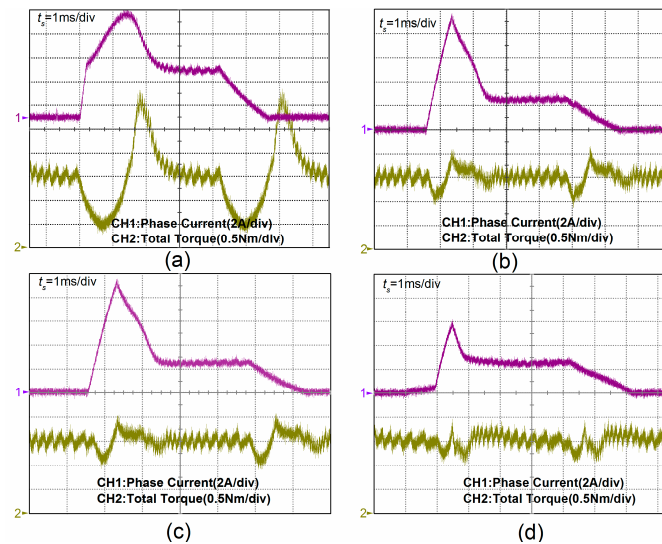424 controller.

Figure 16. Experimental results (speed=3000 rpm, T_{ref}=1.5 Nm): **(a)** CCC; **(b)** Linear TSF; **(c)** Sinusoidal TSF; **(d)** TSF1 (r=4).

Assuming the total electromagnetic torque T is periodic when the actuation current is constant or position-periodic, the total torque T can be extended using a Fourier series as follows:

$$T = t_0 + \sum_{k=1}^{\infty} t_k \cos\left(kN\omega_0 + \varphi_k\right)$$

(19)

where N=3 for the three phases of the 6/4 SRM. Figure 17 (a)-(d) depicts the Fourier analysis of the experimental results of the total torque shown in Figure 16; the units for the phase and amplitude on the y-axis are rad and Nm, respectively. It is evident that the harmonic component of the proposed TSF1 (r=4) is the least. Thus, the results of the simulation and experimental prove that the torque-speed performance and the drive efficiency are significantly improved by using the proposed TSF.
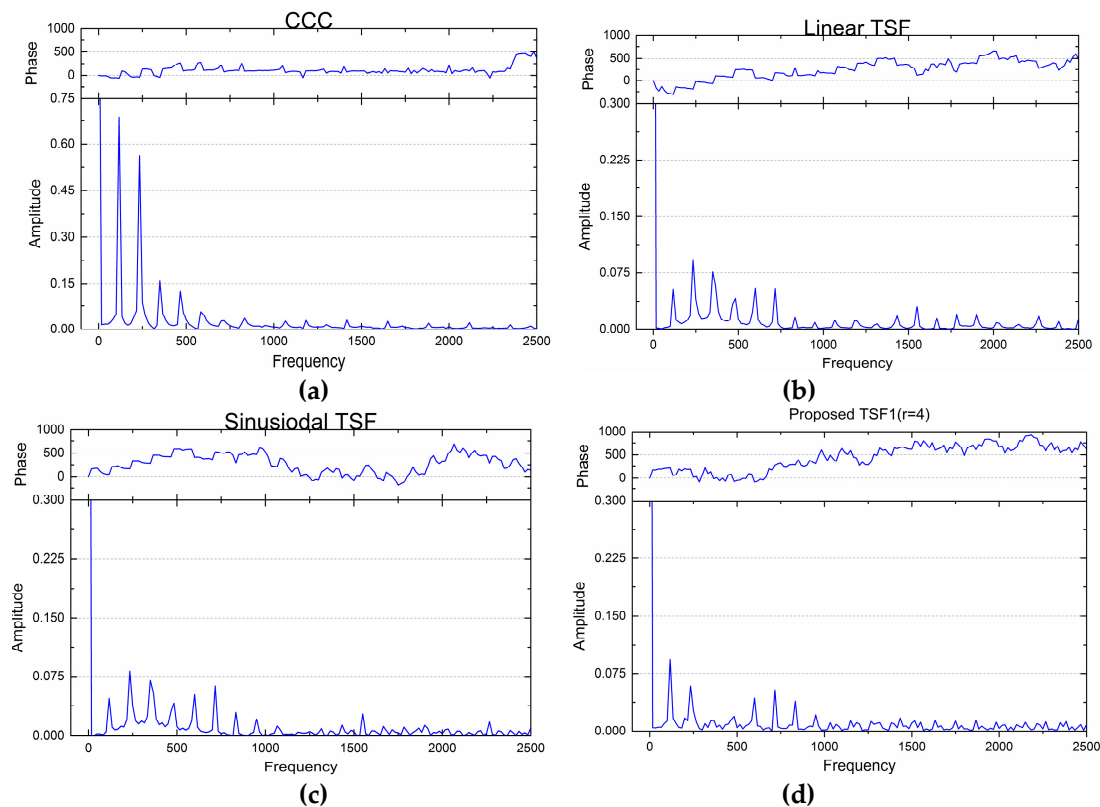

Figure 17. Harmonic component and phase of the total torque (T_{ref}=1.5Nm, speed=3000 rpm): **(a)** CCC; **(b)** Linear TSF; **(c)** Sinusoidal TSF; **(d)** TSF1 (r=4).

9. Conclusion

In this paper, based on the modified optimal criteria with the torque-speed performance and the drive efficiency, a computational procedure for the optimization model of a TSF has been described, including the maximization of the torque-speed range and the minimization of copper loss. In addition, by modifying the optimization objective of the qth-power current, a TSFs family with regard to torque capability is presented and the proposed TSF1 (r=4) is compared with the conventional TSFs. The torque reference can be directly converted into the current reference using the rewritten torque-current profile model of the SRM either in the linear or the saturation magnetic region. The evaluation indices and the performance of the proposed and the classical methods are compared in terms of peak phase current, rms phase current, and torque ripple factor. The experimental results, which match the simulation results very well, show that no matter the rotor speed is low or high, the proposed TSF1 (r=4) has the lowest peak and rms phase current compared with the CCC, the linear, and the sinusoidal TSF. And the proposed TSF1 (r=4) has a commutation torque ripple ratio that is one-third less compared to the conventional TSFs in the saturation magnetic region at a speed of 3000 rpm. Moreover, the proposed TSF1 (r=4) improves the drive efficiency, increases the rotor speed range of the torque-ripple-free operation, and reduces the requirements of the peak and rms phase current. The validity and superiority of the proposed control method are experimentally proved.

Appendix A

Table A1. Parameters of the studied SRM prototype

Stator	6 poles (poles arc:26°)
	Inner diameter: 95 mm
	Outer diameter:150 mm
	Yoke high:12.2 mm
Rotor	4 poles (poles arc:27°)
	Shaft diameter:40 mm
	Yoke high:14.5 mm
Stack length	40 mm
Turns	150 turns/phase
Air gap	0.3 mm
Winding resistor:	0.65 Ω/phase
Type of silicon steel	D25_50

References

1. Krishnan R. Whither motor drives: a case study in switched reluctance motor drives. *International Conference on Electrical Machines and Systems*(*ICEMS2007*), Seoul, South Korea, Oct. 2007, pp. 472-480; Publisher: IEEE.
2. Hannoun H.; Hilairet M.; Marchand C. High performance current control of a switched reluctance machine based on a gain-scheduling PI controller. *Control Engineering Practice*, 2011, vol. 19, pp.1377-1386, DOI: 10.1016/j.conengprac.2011.07.011.
3. Bose B.K. Neural network applications in power electronics and motor drives an introduction and perspective. *IEEE Trans. Ind. Electron.*, 2007, vol.54, no.1, pp.14–33, DOI: 10.1109/TIE.2006.888683.
4. Anwar M.N.; Husain I.; Radun A.V. A comprehensive design methodology for switched reluctance machines. *IEEE Trans. Ind. Appl.*, 2001, vol.37, no.6, pp. 1684-1692, DOI: 10.1109/28.968179.

478   5.   Kalaivani L.; Subburaj P.; Iruthayarajan M.W. Speed control of switched reluctance motor with torque
479   ripple reduction using non-dominated sorting genetic algorithm (NSGA-II). *International Journal of Electrical*
480   *Power and Energy Systems*, 2013, vol.53, pp.69-77, DOI: 10.1016/j.ijepes.2013.04.005.
481   6.   Choi Y.K.; Yoon H.S.; Koh C.S. Pole-shaped optimization of a switched reluctance motor for torque ripple
482   reduction. *IEEE Trans. on Magn.*, 2007, vol. 43, no. 4, pp. 1797-1800, DOI: 10.1109/TMAG.2006.892292.
483   7.   Husain I. Minimization of torque ripple in SRM drives. *IEEE Trans. Ind. Electron.*, 2002, vol. 49, no. 1, pp.
484   28-39, DOI: 10.1109/41.982245.
485   8.   Daryabeigi E.; Dehkordi B.M. Smart bacterial foraging algorithm based controller for speed control of
486   switched reluctance motor drives. *International Journal of Electrical Power and Energy Systems*, 2014, vol.62,
487   pp.364-373, DOI: 10.1016/j.ijepes.2014.04.055.
488   9.   Sahoo S.K.; Panda S.K.; Xu J. Indirect torque control of switched reluctance motors using iterative learning
489   control. *IEEE Trans. Ind. Electron.*, 2005, vol.56, no.8, pp.200-208, DOI: 10.1109/TPEL.2004.839807.
490   10.   Sahoo S.K.; Panda S.K.; Xu J. Iterative learning-based high-performance current controller for switched
491   reluctance motors. *IEEE Trans. Energy Convers.*, 2004, vol.19, no.3, pp. 491-498, DOI:
492   10.1109/TEC.2004.832048.
493   11.   Fuengwarodsakul N.H.; Menne M.; Inderka R.B.; De Doncker R.W. High-dynamic four-quadrant switched
494   reluctance drive based on DITC. *IEEE Trans. Ind. Appl.*, 2005, vol.41, no.5, pp. 1232-1242, DOI:
495   10.1109/TIA.2005.853381.
496   12.   Inderka R.B.; De Doncker R.W. DITC-Direct instantaneous torque control of switched reluctance drives.
497   *IEEE Trans. Ind. Appl.*, 2003, vol.39, no.4, pp. 1046-1051, DOI: 10.1109/TIA.2003.814578.
498   13.   Hannoun H.; Hilairet M.; Marchand C. Design of an SRM speed control strategy for a wide range of
499   operating speeds. *IEEE Trans. Ind. Electron.*, 2010, vol.57, no.9, pp.2911-2921, DOI:
500   10.1109/TIE.2009.2038396.
501   14.   Mademlis C.; Kioskeridis I. Performance optimization in switched reluctance motor drives with online
502   commutation angle control. *IEEE Trans. Energy Convers.*, 2003, vol.18, no.3, pp.448-457, DOI:
503   10.1109/TEC.2003.815854.
504   15.   Husain I.; Hossain S.A. Modeling, simulation, and control of switched reluctance motor drives. *IEEE Trans.*
505   *Ind. Electron.*, 2005, vol.52, no.6, pp. 1625-1634, DOI: 10.1109/TIE.2005.858710.
506   16.   Sahoo S.K.; Dasgupta S.; Panda S.K.; Xu J. A Lyapunov function based robust direct torque controller for a
507   switched reluctance motor drive system. *IEEE Trans. Power Electron.*, 2012, vol.27, no.2, pp.555-564, DOI:
508   10.1109/TPEL.2011.2132740.
509   17.   Mikail R.; Husain I.; Sozer Y.; Islam M.; Sebastain T. Torque-ripple minimization of switched reluctance
510   machines through current profiling. *IEEE Trans. Ind. Appl.*, 2013, vol.49, no.3, pp.1258-1267, DOI:
511   10.1109/TIA.2013.2252592.
512   18.   Shaked N.T.; Rabinovici R. New procedures for minimizing the torque ripple in switched reluctance motors
513   by optimizing the phase-current profile. *IEEE Trans. Magn.*, 2005, vol.41, no.3, pp. 1184-1192, DOI:
514   10.1109/TMAG.2004.843311.
515   19.   Xue X.D.; Cheng K.W.E.; Ho S.L. Optimization and evaluation of torque sharing function for torque ripple
516   minimization in switched reluctance motor drives. *IEEE Trans. Power Electron.*, 2009, vol.24, no.9, pp.2076-
517   2090, DOI: 10.1109/TPEL.2009.2019581.
518   20.   Pop A.C.; Petrus V.; Martis C.S.; and et al. Comparative study of different torque sharing functions for
519   losses minization in switched reluctance motors used in electric vehicles propulsion. *Proceedings of 13th*
520   *International Conference on Optimization of Electrical and Electronic Equipment (OPTIM)*, Brasov, Romania,
521   May 2012, pp. 356-365; Publisher: IEEE.
522   21.   Ye J.; Bilgin B.; Emadi A. An offline torque sharing function for torque ripple reduction in switched
523   reluctance motor drives. *IEEE Trans. Energy Convers.*, 2015, vol.30, no.2, pp.726-735. DOI:
524   10.1109/TEC.2014.2383991.
525   22.   Ye J.; Bilgin B.; Emadi A. An extended-speed low-ripple torque control of switched reluctance motor drives.
526   *IEEE Trans. Power Electron.*, 2015, vol.30, no.3, pp.1457-1470, DOI: 10.1109/TPEL.2014.2316272.
527   23.   Lee D.H.; Lee Z.G.; Ahn J.W. A simple nonlinear logical torque sharing function for low-torque ripple SR
528   drive. *IEEE Trans. Ind. Electron.*, 2009, vol.56, no.8, pp. 3021-3028, DOI: 10.1109/TIE.2009.2024661.
529   24.   Dowlatshahi M.; Nejad S.M.S.; Moallem M.; Ahn J.W. Torque ripple reduction of switched reluctance
530   motors considering copper loss minimization. *2014 IEEE International Conference on Industrial Technology*
531   *(ICIT2014)*, Busan, South Korea, Feb./Mar. 2014, pp.858-865; Publisher: IEEE.

532   25.   Dowlatshahi M.; Nejad S.M.S.; Ahn J.W.; Moallem M. Copper loss and torque ripple minimization in
533   switched reluctance motors considering nonlinear and magnetic saturation effects. *Journal of Power*
534   *Electronics*, 2014, vol.14, no.2, pp.351-361, DOI: 10.6113/JPE.2014.14.2.351.
535   26.   Vujičić V.P. Modeling of a switched reluctance machine based on the invertible torque function. *IEEE Trans.*
536   *Magn.*, 2008, vol.44, no.9, pp. 2186- 2194, DOI: 10.1109/TMAG.2008.2000663.
537   27.   Xue X.D.; Cheng K.W.E.; Ho S.L. Study of power factor in SRM drives under current hysteresis chopping
538   control. *Fourtieth IAS Annual Meeting, Conference Record of the 2005 Industry Applications Conference*,
539   Kowloon, Hong Kong, China, Oct. 2005, vol.4, pp.2734-2740; Publisher: IEEE.